crystals

MDPI

*Article*

# Microstructural Investigation and High-Temperature Oxidation Performance of K417G Alloy Prepared by Wide-Gap Brazing

**Zhun Cheng [1,*], Xin Lai [1], Jing He [1], Xiaoqiang Li [2,*], Jiafeng Fan [2] and Fuqiang Lai [3]**

[1] Guangdong Polytechnic of Industry and Commerce, Guangzhou 510510, China; laixin1@gdgmzyjsxy4.wecom.work (X.L.); hejing_1127@gdgm.edu.cn (J.H.)
[2] Guangdong Key Laboratory for Advanced Metallic Materials Fabrication and Forming, National Engineering Research Center of Near-Net-Shape Forming for Metallic Materials, South China University of Technology, Guangzhou 510640, China; 202110180443@mail.scut.edu.cn
[3] School of Mechanical Engineering and Automation, Fuzhou University, Fuzhou 350116, China; laifuqiang@fzu.edu.cn
* Correspondence: chengzhun@gdgm.edu.cn (Z.C.); lixq@scut.edu.cn (X.L.)

**Abstract:** K417G superalloy is widely applied in gas turbine components such as blades, vanes, and nozzles. In this work, the oxidation behavior and mechanism of K417G alloy prepared by wide-gap brazing were investigated in air at 800, 900, 1000, and 1100 °C. Microstructures of the bonded joints differ in the wide-gap braze region (WGBR) and base metal (BM). The surface and cross-sectional morphology, composition, and structure of specimens were analyzed by XRD, SEM, and EDS after oxidation tests. The experimental data demonstrate that the WGBR (wide-gap brazed region) exhibits markedly superior oxidation resistance compared to the BM (base material) under elevated-temperature conditions exceeding 1000 °C. This performance disparity is quantitatively validated by oxidation kinetics analysis, where the weight gain curve of the WGBR demonstrates parabolic oxidation kinetics, as evidenced by its significantly lower parabolic rate constant relative to the BM. The oxide layers of the BM and WGBR are similar after oxidation at high temperatures of 800–900 °C, and they consist of an outermost layer of NiO, a middle mixed layer of $Cr_2O_3$, and an innermost layer of dendritic $Al_2O_3$. However, when the temperature is between 1000 and 1100 °C, the NiO on the surface of the BM spalls of due to thermal expansion coefficient mismatch in coarse-grained regions, resulting in oxidation mainly divided into outer layer $Cr_2O_3$ and inner layer $Al_2O_3$ and $TiO_2$. Under high-temperature oxidation conditions (1000–1100 °C), a structural transition occurs in the oxide scale of the BM, with the underlying mechanism attributable to grain-coarsening-induced oxide scale destabilization. Specifically, the coarse-grained structure of the BM (characteristic grain size exceeding 50 μm) is exhibited. Therefore, the WGBR demonstrates outstanding oxidation resistance, as evidenced by the formation of a continuous $Al_2O_3$ scale with parabolic rate constants of about $1.38 \times 10^{-3}$ $mg^2 \cdot cm^{-4} \cdot min^{-1}$ at 1100 °C.

**Keywords:** K417G alloy; oxidation resistance; microstructures; oxidation layer

check for updates

Academic Editor: Benilde F. O. Costa

Received: 16 April 2025
Revised: 29 April 2025
Accepted: 1 May 2025
Published: 2 May 2025

**Citation:** Cheng, Z.; Lai, X.; He, J.; Li, X.; Fan, J.; Lai, F. Microstructural Investigation and High-Temperature Oxidation Performance of K417G Alloy Prepared by Wide-Gap Brazing. *Crystals* **2025**, *15*, 434. https://doi.org/10.3390/cryst15050434

**Copyright:** © 2025 by the authors. Licensee MDPI, Basel, Switzerland. This article is an open access article distributed under the terms and conditions of the Creative Commons Attribution (CC BY) license (https://creativecommons.org/licenses/by/4.0/).

## 1. Introduction

K417G superalloy is a nickel-based precipitation-hardened cast superalloy [1]. It was initially developed by the Institute of Metal Research, Chinese Academy of Sciences, as a replica of the American IN100 superalloy, resulting in the successful creation of the K417 cast superalloy. Subsequently, the K417G alloy was further developed, exhibiting advantages such as low density, high intermediate-temperature strength, good plasticity, and excellent

corrosion resistance. As a result, it has been widely used in hot-section components of aero-engines, such as turbine blades and guide vanes [2–5]. In recent years, with the rapid and sustained development of industrial production, hot-section components are subjected to long-term service in harsh environments involving high temperatures and gas flow, making them highly susceptible to the initiation and propagation of microcracks into large-gap cracks. Therefore, the high-quality repair of large-gap cracks in high-temperature components has become a critical method for extending equipment service life [6].

Currently, the primary technique for repairing large-gap cracks in superalloys is wide-gap brazing technology [7]. This method is based on the Transient Liquid Phase (TLP) bonding principle, where the filler material consists of a small amount of low-melting-point alloy containing melting point depressants (MPDs) and a high-melting-point alloy with a composition close to that of the base metal. Cheng et al. [8] studied the wide-gap brazing of K417G alloy with low-melting-point nickel-based alloy powder containing boron (LMP) and high-melting-point nickel-based alloy powder (HMP). The effect of the composition of filler metal on microstructure evolution and mechanical properties of the joint was analyzed, and the strengthening mechanism of the joint was investigated. When the ratio of HMP in the filler metal increases to 95 wt%, B can be uniformly diffused into the HMP, and dispersed granular $M_3B_2$ borides at the interface are obtained. The tensile strength of the joint at room temperature and 600 °C is 971 and 934 MPa, respectively, reaching the strength of the base metal. Ren [9] reported the microstructure evolution and mechanical properties of wide-gap brazed K417G superalloy joints with BNi-5 filler alloy and additive superalloy powders. The brazing experiment was conducted at 1200 °C for 30 min. B atoms uniformly diffused through the K417G alloy and additive alloy. The interfacial evolution and diffusion behavior were investigated. With the prolonging of the holding time, a stronger mutual element diffusion phenomenon occurred. The joints brazed at 1150 °C for 30 min exhibit the highest average tensile strength of 404 MPa tested at 950 °C.

However, during the service of aero-engines, repaired hot-section components such as turbine blades endure complex and extreme working conditions, including high temperatures, high pressure, and high rotational speeds [10]. Consequently, the repaired components are prone to high-temperature oxidation, which leads to surface depletion of strengthening elements, loss of strength, and crack initiation, ultimately resulting in component failure. Thus, oxidation resistance has become one of the key indicators for evaluating the repair performance of superalloys [11]. Revealing the initial oxidation behavior of K417G superalloys is significant for a better understanding of the oxidation mechanism of turbine blades during service conditions. High-temperature oxidation testing under atmospheric conditions is the most commonly used method for assessing the oxidation behavior of superalloys [12,13]. Different design approaches for wide-gap brazing of superalloys result in variations in service temperature and performance. However, research on their oxidation behavior and the underlying differences remains limited.

This study focuses on the oxidation resistance of wide-gap brazed K417G alloy at 800 °C, 900 °C, 1000 °C, and 1100 °C. It systematically investigates the oxidation kinetics, phase composition of oxide layers, surface morphology, and cross-sectional microstructure, explores the high-temperature oxidation mechanisms, and provides a theoretical foundation for optimizing the comprehensive performance of large-gap powder-metallurgy-bonded joints.

## 2. Experimental Section

### *2.1. Materials and Sample Preparation*

The microstructures of the bonded specimens were measured by NOVA NANOSEM 430 field emission Electron Backscatter Diffraction (EBSD). The EBSD data were analyzed

using the Channel 5 software. Figure 1a,b reveal that the joint primarily consists of the base metal (BM) region and the wide-gap brazed region (WGBR). The BM exhibits coarse grains of 2–5 mm, resulting from the casting process (Figure 1c). The BM region contains a $\gamma$-austenite matrix, $\gamma'$ precipitates, $\gamma/\gamma'$ eutectic structures, and MC-type carbides as its main phases [14,15]. In contrast, as shown in Figure 1d, the WGBR displays fine grains ranging from 20 to 100 µm. This refined grain structure is attributed to the powder sintering process, where the grain size may correlate with the initial powder particle size. The WGBR predominantly comprises the same matrix phases as the BM ($\gamma$-austenite matrix and $\gamma'$ precipitates), along with $M_3B_2$ white boride particles, while $\gamma/\gamma'$ eutectic structures are absent [16].

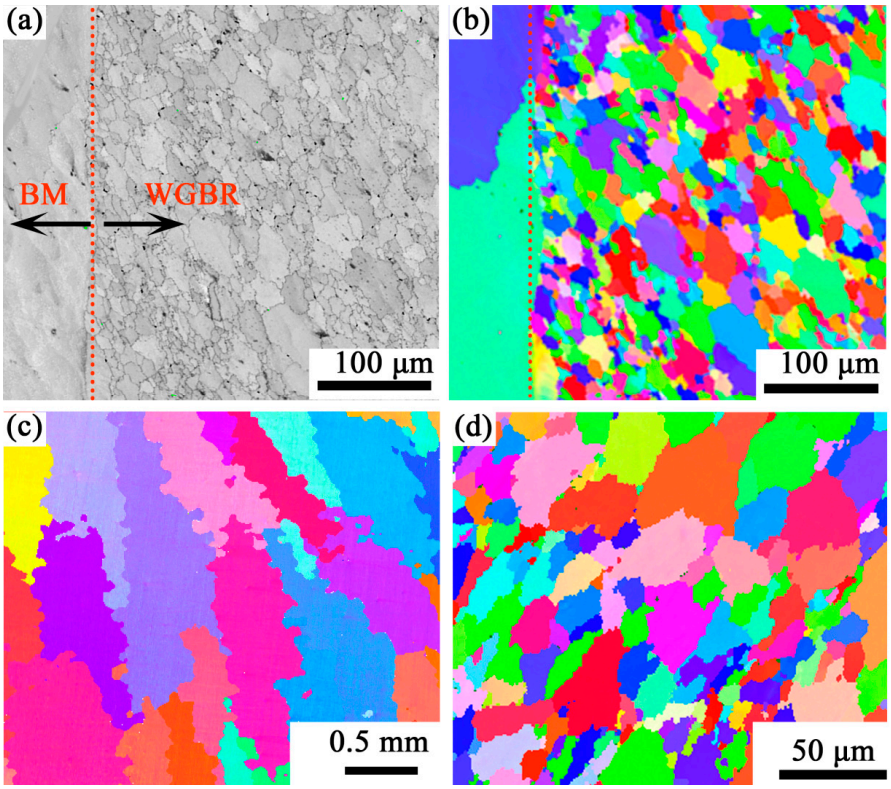


**Figure 1.** Backscattered Electron Micrograph (**a**) and EBSD image (**b**) of the wide-gap brazing joint, (**c**) EBSD image of the BM, (**d**) EBSD image of the WGBR. The red dashed line indicates the interface region between the BM and WGBR.

### *2.2. Oxidation Tests*

Circular specimens with dimensions of Φ4 × 3 mm were sectioned from the BM, joint interface, and WGBR. The specimens were first ground with 800 grit sandpaper, mechanically polished, and then ultrasonically cleaned three times in a mixed solution of alcohol and acetone, followed by drying. Isothermal oxidation experiments were conducted using a simultaneous thermal analyzer (STA 449C, DSC/TGA). The heating rate was set to 20 °C/min. Prior to the target oxidation temperatures (800 °C, 900 °C, 1000 °C, and 1100 °C) being reached, inert argon gas was purged to protect the specimens from pre-oxidation. Upon reaching the target temperatures, a mixed gas containing 79% $N_2$ and 21% $O_2$ (simulating air composition) was introduced for isothermal oxidation over 1440 min.

### *2.3. Microstructural Characterization*

The surface and cross-sectional morphologies of the oxide layers were examined using a scanning electron microscope (SEM, XL-30 FEG), while their chemical compositions were

analyzed via energy-dispersive spectroscopy (EDS, Oxford X-max 80). The distribution of major elements within the oxide layers was characterized by electron probe microanalysis (EPMA, JXA-8230). Phase identification and quantification were carried out by X-ray diffraction (XRD) on an STOE STADI P diffractometer (STOE & Cie. GmbH) using Mo $K_{\alpha 1}$ radiation (λ = 0.7093 Å). The step size was 0.02°, the scanning speed was 0.05°/min, and the scanning range was 20–80°. A TEM sample of a cross-section of oxide film was prepared by an FEI Helios Nanolab 600 focused ion beam (FIB) microscope. The crystal structure of the oxide film was identified by a JEM-2100F transmission electron microscope (TEM).

## 3. Results

### *3.1. Oxidation Behaviors at High Temperature*

Figure 2 shows the isothermal oxidation kinetics curves of the BM and WGBR at 800 °C, 900 °C, 1000 °C, and 1100 °C. The results indicate that the oxidation process of the superalloy primarily consists of two stages: an initial rapid oxidation phase followed by a stabilized oxidation phase. This behavior can be attributed to the following mechanisms:

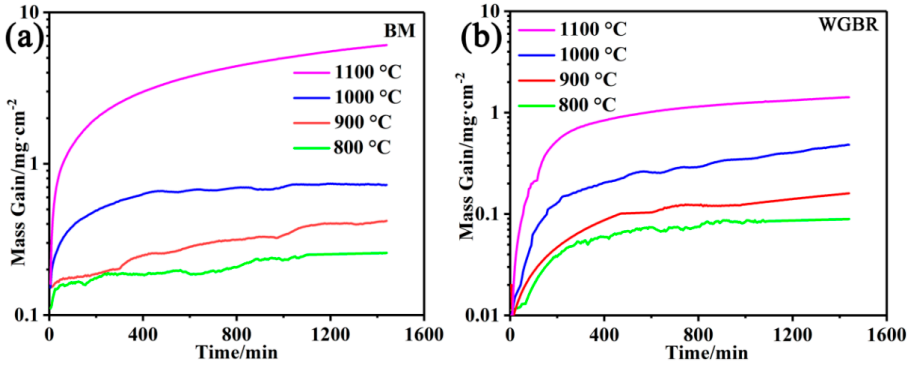


**Figure 2.** Oxidation kinetic curves of the BM (**a**) and WGBR (**b**).

Initial stage: Oxygen directly reacts with surface elements to form oxides or oxide films, leading to a high oxidation rate.

Later stage: Reactants combine through the diffusion of cations and anions across the oxide layer, rendering the oxidation rate diffusion-controlled and consequently slower.

This observation aligns with previous reports [17]. The oxidation behavior of the tested alloy follows the same trend and adheres to a parabolic law, as illustrated in Figure 3. Specifically, rapid mass gain occurs during the initial stage, while the oxidation rate gradually decreases over time. The accelerated initial oxidation is driven by oxide nucleation at surface defects (e.g., grain boundaries), whereas the subsequent rate reduction reflects the transition to diffusion-controlled kinetics as nucleation sites diminish.

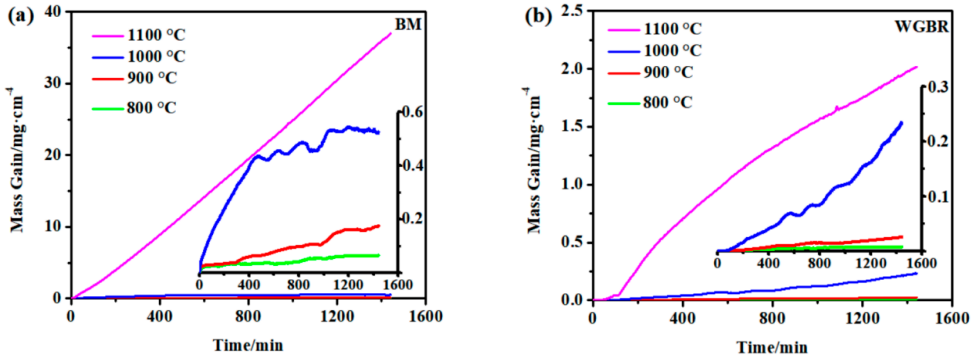


**Figure 3.** Oxidizing dynamic curves of the BM (**a**) and WGBR (**b**).

Additionally, the oxidation rates of both the BM and WGBR increase significantly with temperature. Notably, the BM exhibits a relatively low oxidation rate below 1000 °C, with an average rate of $0.50 \times 10^{-3}$ mg·cm$^{-2}$·min$^{-1}$ after 1440 min at 1000 °C. However, this value surges to $42.24 \times 10^{-3}$ mg·cm$^{-2}$·min$^{-1}$ at 1100 °C, representing a two-order-of-magnitude increase (see Table 1). In contrast, the WGBR demonstrates a much lower oxidation rate of $1.00 \times 10^{-3}$ mg·cm$^{-2}$·min$^{-1}$ at 1100 °C. Furthermore, the WGBR exhibits slow mass gain and no oxide spallation after 1440 min at 1100 °C, whereas the BM suffers from severe oxide layer detachment. These findings confirm that the BM undergoes more pronounced oxidation than the WGBR under identical conditions.

**Table 1.** Oxidation rate of the BM and WGBR.

| Sample | Oxidation Rate (mg·cm$^{-2}$·h$^{-1}$) | | | |
|---|---|---|---|---|
| | 800 °C | 900 °C | 1000 °C | 1100 °C |
| BM | 0.18 × 10−3 | 0.29 × 10−3 | 0.50 × 10−3 | 42.24 × 10−3 |
| WGBR | 0.06 × 10−3 | 0.16 × 10−3 | 0.35 × 10−3 | 1.00 × 10−3 |

According to oxidation kinetics theory, the oxidation rate of metals is controlled by the diffusion of oxygen ions and metal ions through the oxide layer, which can be expressed as follows:

$$K_p = \frac{\Delta m^2}{t} \quad (1)$$

In the equation, $K_p$ represents the parabolic rate constant, $\Delta m$ denotes the mass gain per unit area, and $t$ is the oxidation time. The calculated results (Table 2) show that the oxidation rate constants of both the BM and WGBR at 1100 °C are significantly higher than those at 800 °C, 900 °C, and 1000 °C. Notably, $K_{p\text{-WGBR}}$ exceeds $K_{p\text{-BM}}$ at 800–1000 °C, whereas $K_{p\text{-BM}}$ becomes markedly greater than $K_{p\text{-WGBR}}$ at 1100 °C. This indicates that the oxide layer of the WGBR exhibits superior high-temperature oxidation resistance at temperatures up to 1000 °C, effectively reducing the oxidation rate.

**Table 2.** Parabolic rate constants $K$p of the BM and WGBR (mg$^2$·cm$^{-4}$·min$^{-1}$).

| Sample | $K_p$ (mg$^2$·cm$^{-4}$·min$^{-1}$) | | | |
|---|---|---|---|---|
| | 800 °C | 900 °C | 1000 °C | 1100 °C |
| BM | $1.01 \times 10^{-5}$ | $1.85 \times 10^{-5}$ | $1.31 \times 10^{-4}$ | $2.78 \times 10^{-2}$ |
| WGBR | $2.07 \times 10^{-6}$ | $2.25 \times 10^{-5}$ | $2.73 \times 10^{-4}$ | $1.38 \times 10^{-3}$ |

Furthermore, the $K$p value of the WGBR exhibits significant temperature dependence, increasing by an order of magnitude for every 100 °C rise in temperature. A comparison with the literature [18] reveals that the oxidation rate constant of the WGBR closely approximates the growth rate constant of $Cr_2O_3$. Consequently, the diffusion activation energies of $O^{2-}$ and $Cr^{3+}$ ions were calculated. Since elemental diffusion is a thermally activated process, it follows the Arrhenius equation:

$$K_p = K_0 exp\left(-\frac{Q}{RT}\right) \quad (2)$$

where the following definitions hold:

$K_0$ = Pre-exponential constant;
$Q$ = Activation energy (430 kJ/mol for the alloy);
$R$ = Universal gas constant;
$T$ = Absolute temperature.

The calculated activation energy $Q$ of the alloy is 430 kJ/mol, which matches the diffusion activation energy of $O^{2-}$ ions in $Cr_2O_3$ films. This confirms that the oxidation process of the WGBR is predominantly controlled by the inward diffusion of $O^{2-}$ ions.

### *3.2. Oxide Composition*

Within the temperature range of 800–1000 °C, the high-temperature oxidation behavior of the BM and WGBR are fundamentally similar.

Figure 4 illustrates the surface oxide compositions of the BM and WGBR after 1440 min of oxidation at 1000 °C. As shown in Figure 4a, the oxide layer on the BM primarily consists of NiO, $TiO_2$, and $Cr_2O_3$ after 1440 min of isothermal oxidation. Previous studies [19] have reported that NiO and $Cr_2O_3$ in the oxide layer of K417G alloy begin to form at 800 °C. With increasing temperature, Ti elements from the substrate continuously diffuse outward through the oxide layer and are oxidized to form $TiO_2$.

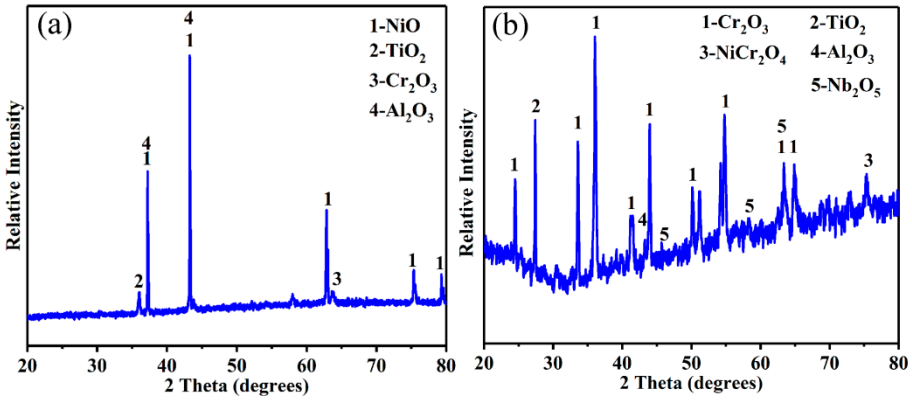


**Figure 4.** XRD patterns of the BM (**a**) and WGBR (**b**) after oxidation at 1000 °C for 1440 min.

In contrast, Figure 4b demonstrates that the oxide layer on the WGBR is predominantly composed of $Cr_2O_3$, $NiCr_2O_4$, and $TiO_2$. This indicates that the WGBR preferentially forms oxides such as $NiCr_2O_4$ and $Cr_2O_3$ under these conditions, showing a distinct compositional difference compared to the BM. This difference may be attributed to the presence of multiple active elements (e.g., Al and Ti) in the WGBR, which collectively participate in the oxidation reactions. These elements reduce the oxidation propensity of Ni, resulting in minimal NiO formation in the WGBR oxide layer.

### *3.3. Surface Morphology of Oxidized Material*

Figure 5 displays the surface oxide morphologies of the large-gap powder-metallurgy-bonded joint after 1440 min of oxidation at 1000 °C. Macroscopic observations reveal that the oxide layer on the WGBR is significantly denser, whereas interparticle gaps persist in the oxide layer of the BM.

Figure 6 shows the oxide morphologies of the BM oxidized for 1440 min at 800 °C, 900 °C, 1000 °C, and 1100 °C. After oxidation at 800 °C, the BM oxide layer exhibits a granular surface morphology. Based on the XRD results in Figure 4a, these granular oxides are likely composite phases of NiO, $TiO_2$, and $Cr_2O_3$. Upon oxidation at 1000 °C, the surface oxides on the BM grow markedly, forming large nodular oxide clusters. These nodular oxides are composed of aggregated fine spherical particles, which, combined with XRD analysis, are hypothesized to be mixtures of NiO and $TiO_2$. As shown in Figure 6d, the oxide layer on the BM undergoes fragmentation, likely caused by thermal expansion coefficient mismatch between different oxides, leading to crack formation.

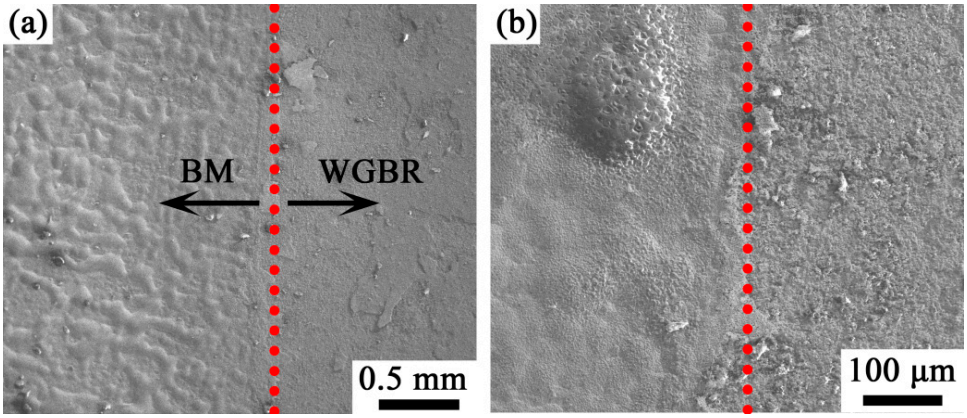


**Figure 5.** Low-magnification (**a**) and High-magnification (**b**) SEM images of the oxide scales of the joint after oxidation for 1440 min at 1000 °C. The red dashed line indicates the interface region between the BM and WGBR.

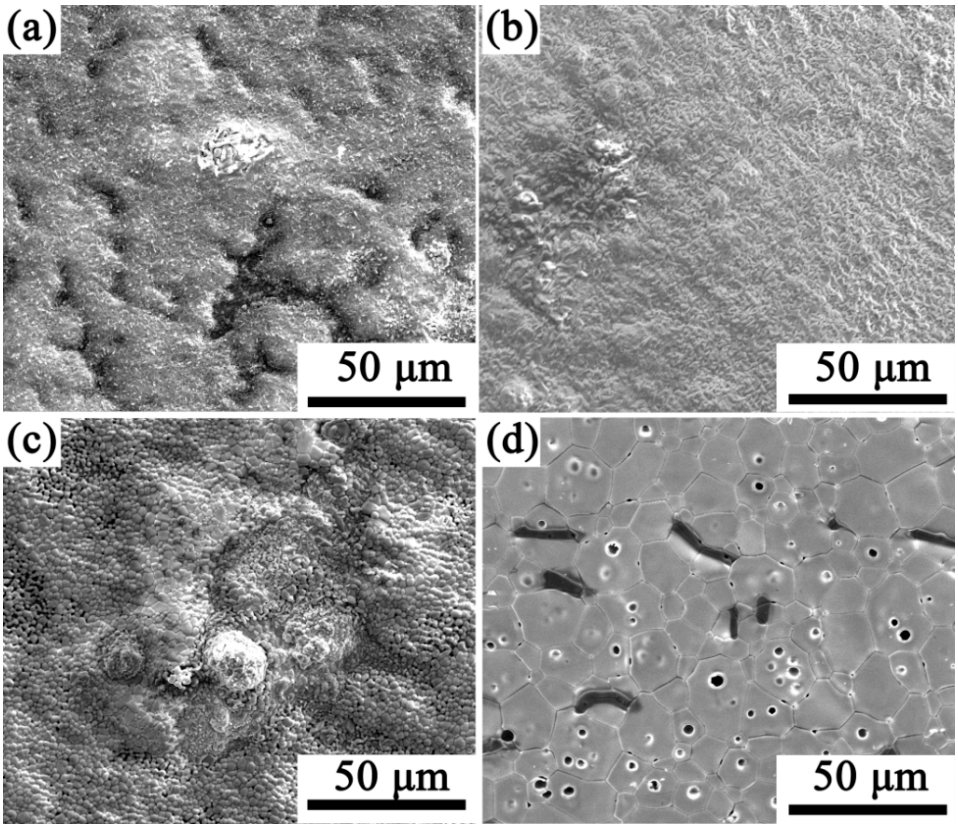


**Figure 6.** SEM images of the oxide scales of the BM after oxidation for 1440 min at 800 °C (**a**), 900 °C (**b**), 1000 °C (**c**) and 1100 °C (**d**).

Figure 7 presents the oxide layer morphologies of the WGBR after 1440 min of oxidation at 800 °C, 900 °C, 1000 °C, and 1100 °C. At 800 °C, minimal oxide formation is observed on the WGBR surface. Oxidation at 900 °C yields a uniformly distributed oxide layer. However, localized spallation occurs in the oxide layer at 1000 °C. Based on XRD analysis, the intact regions likely consist of densely structured $Cr_2O_3$, while the spalled areas may correspond to secondary oxides formed via elemental diffusion. At 1100 °C, severe oxide spallation significantly compromises the oxidation resistance of the WGBR.

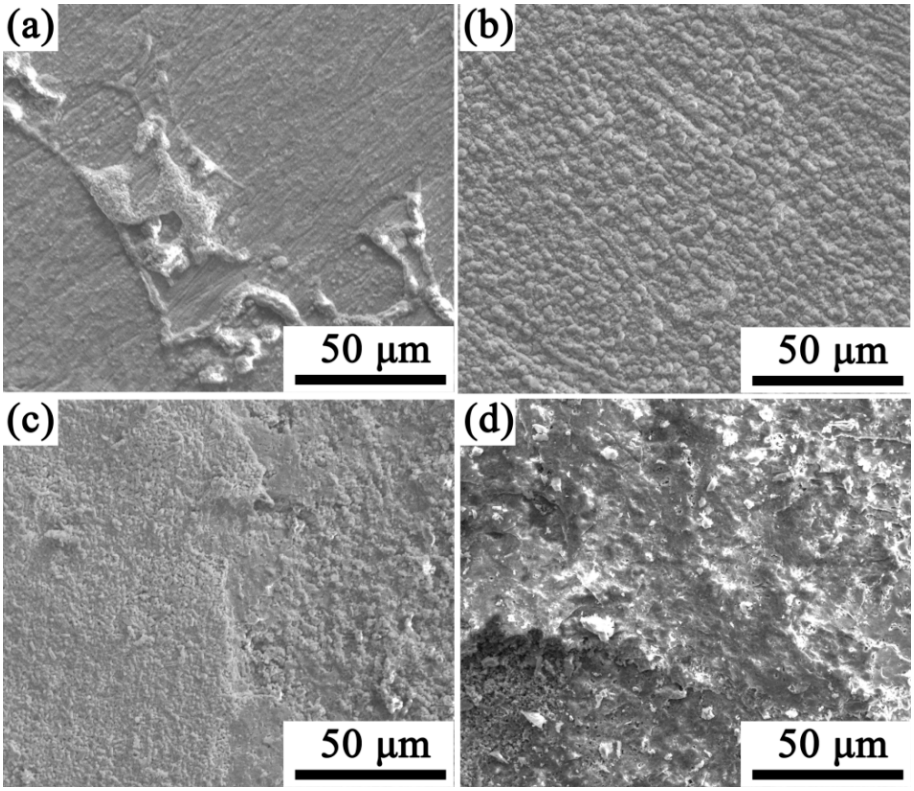


**Figure 7.** SEM images of the oxide scales of the WGBR after oxidation for 1440 min at 800 °C (**a**), 900 °C (**b**), 1000 °C (**c**), and 1100 °C (**d**).

An analysis of the literature [20,21] suggests that the primary cause of oxide spallation is the excessive internal stresses generated within the dense $Cr_2O_3$ and $NiCr_2O_4$ layers formed on the WGBR during oxidation. Generally, these internal stresses originate from two sources:

Growth stress: Resulting from the mismatch in Pilling–Bedworth (PB) ratios between $NiCr_2O_4$ and $Cr_2O_3$, reflecting the volume ratio of oxides to their parent metals.

Thermal stress: Arising from differences in thermal expansion coefficients between $NiCr_2O_4$ and $Cr_2O_3$, leading to differential volume changes during heating or cooling cycles.

The combined effects of these stresses induce significant interfacial stresses between the oxides, ultimately causing localized spallation of the oxide layer from the $Cr_2O_3$ matrix.

### *3.4. Cross-Sectional Morphology After High-Temperature Oxidation*

A comprehensive evaluation of the alloy's oxidation resistance can be achieved by analyzing the mass gain before and after oxidation, phase evolution, and interfacial morphology of the oxide layers. Figure 8 illustrates the cross-sectional morphology of the wide-gap brazed joint after 1440 min of oxidation. Under identical temperature and isothermal duration conditions, the oxide layer on the BM is markedly thicker than that on the WGBR.

Figure 9 shows the cross-sectional morphologies of the BM after 1440 min of oxidation at various temperatures. At 800 °C, a thin, continuous oxide layer with a porous structure forms on the BM surface, exhibiting crack-like pores and an average thickness of 2.28 μm. As the oxidation temperature increases, the oxide layer thickness changes significantly. At 1000 °C, the thickness increases to 6.78 μm, with pore quantity and size substantially larger than those at 800 °C. These pores likely initiate and propagate cracks, particularly under cyclic stress. At 1100 °C, the oxide layer thickens dramatically to 30.41 μm. Overall, BM

undergoes primarily surface oxidation due to the dense, continuous inner oxide layer that prevents internal oxidation, leading to thick outer oxide formation.

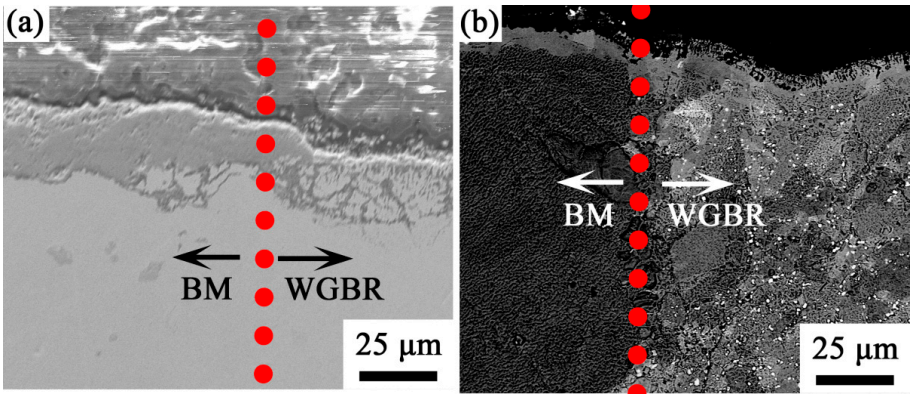


**Figure 8.** Scanning Electron Microscope Micrograph (**a**) and Backscattered Electron Micrograph (**b**) of cross-section of joint oxidized at 1000 °C for 1440 min. The red dashed line indicates the interface region between the BM and WGBR.

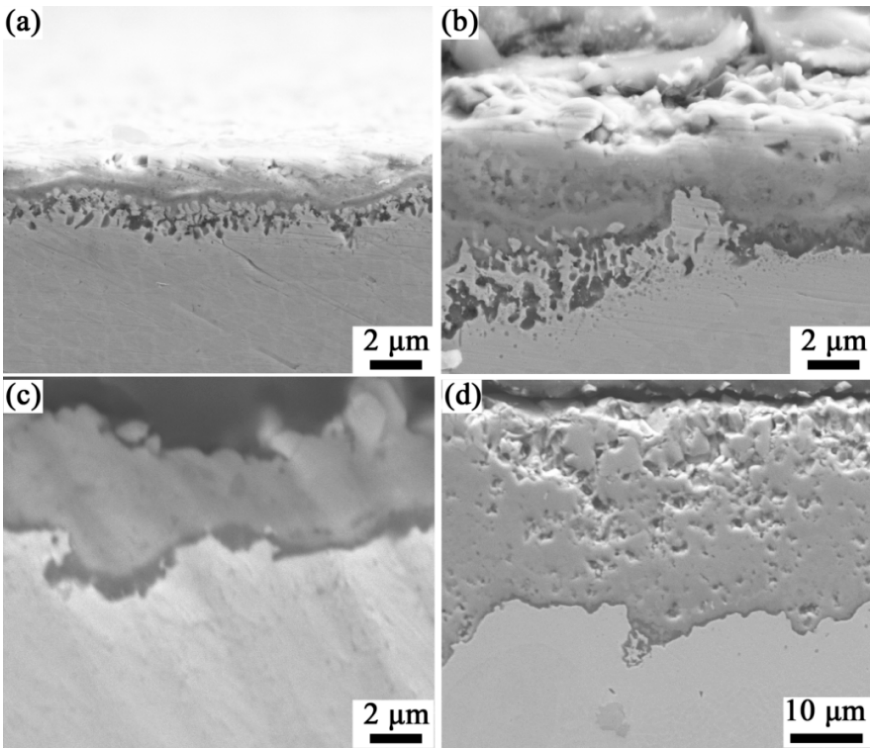


**Figure 9.** SEM images of a cross-section of the BM after oxidation at 800 °C (**a**), 900 °C (**b**), 1000 °C (**c**) and 1100 °C (**d**) for 1440 min.

Figure 10 displays the cross-sectional morphologies of the WGBR after 1440 min of oxidation. At 800 °C, the layered oxide structure averages 2.08 μm in thickness, thinner than the BM. Consistent with the BM's oxidation behavior, the oxide layer at 1000 °C thickens to 5.53 μm, with larger and more numerous pores. At 1100 °C, the thickness reaches 30.05 μm. This accelerated oxidation in the WGBR may stem from its abundant grain boundaries, which facilitate inward oxygen diffusion and outward alloy element diffusion. The literature [22] notes that internal oxidation proceeds slower than surface oxidation, explaining why the BM's oxide layer is thicker than the WGBR's under identical conditions.

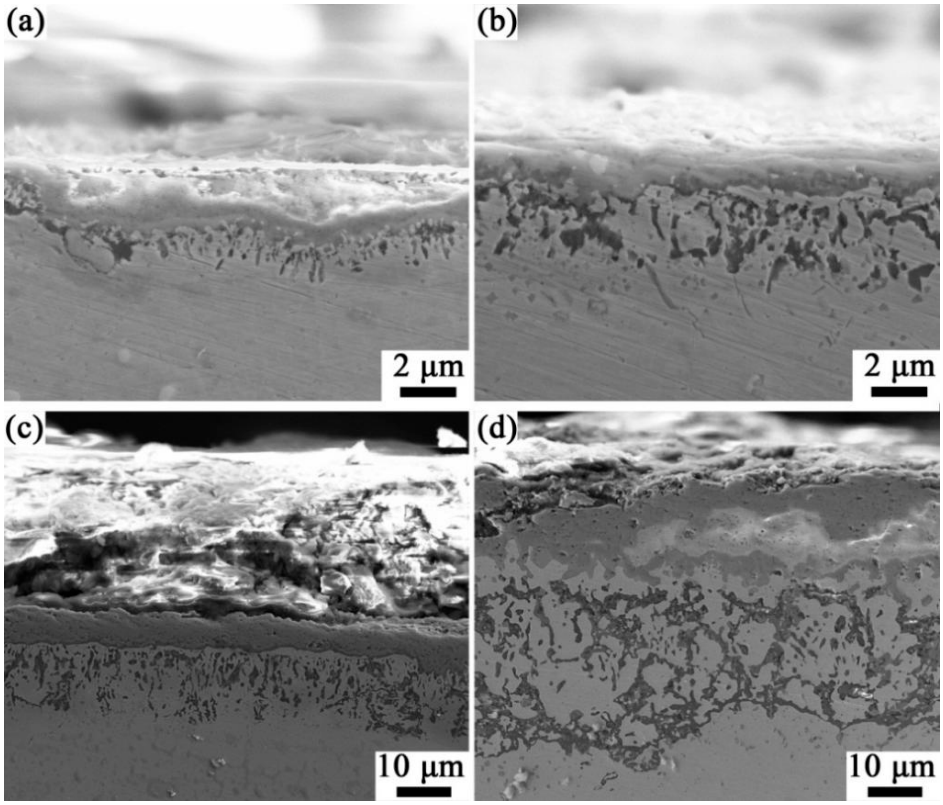


**Figure 10.** SEM images of a cross-section of the WGBR oxidized at 800 °C (**a**), 900 °C (**b**), 1000 °C (**c**), and 1100 °C (**d**) for 1440 min.

Figure 11 presents the cross-sectional morphology and EDS elemental maps of the BM oxidized at 1000 °C for 1440 min. The oxide layer comprises three distinct regions:

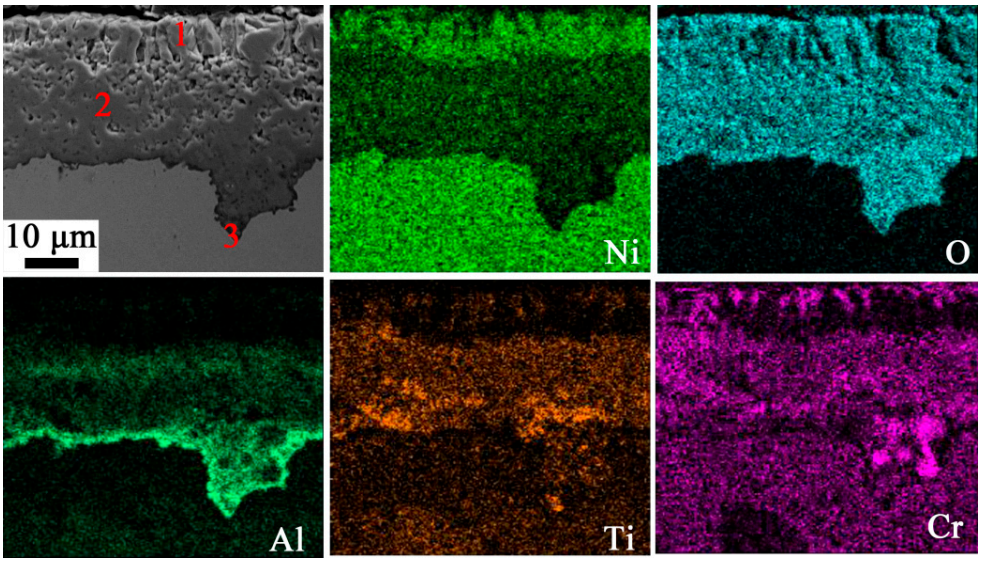


**Figure 11.** SEM images of a cross-section and EDS element mapping of the BM oxidized at 1000 °C for 1440 min. Point 1 corresponds to the outermost dendritic oxide, Point 2 represents the intermediate gray oxide layer, and Point 3 denotes the innermost dark gray oxide region.

Outer layer: Enriched with Ni (likely NiO and minor $Cr_2O_3$, based on XRD and EDS data in Table 3).

**Table 3.** EDS analysis of the oxide scales in Figure 11 (at.%).

| Spots | Element (at.%) | | | | | | |
|---|---|---|---|---|---|---|---|
| | O | Al | Ti | Cr | Co | Ni | Mo |
| 1 | 21.17 | 1.03 | 3.37 | 7.16 | 7.47 | 37.07 | 1.31 |
| 2 | 47.72 | 11.72 | 5.83 | 8.32 | 5.86 | 19.58 | 0.98 |
| 3 | 50.30 | 38.38 | 0.61 | 1.77 | 0.98 | 7.24 | 2.87 |

Intermediate layer: A dense mixture of $TiO_2$ and $Cr_2O_3$.

Inner layer: A thin $Al_2O_3$ film undetected by XRD due to its depth.

The oxide/substrate interface shows strong adhesion, with localized substrate protrusions embedded into the oxide layer. Studies [23] suggest that vacancies form at the $Cr_2O_3$/substrate interface as Ni, Nb, and Cr ions diffuse outward. However, uniform $Al_2O_3$ formation in BM suppresses vacancy aggregation, preventing microvoid formation and enhancing oxide adhesion.

Figure 12 illustrates the cross-sectional morphology and EDS maps of the WGBR oxidized at 1000 °C for 1440 min. The oxide layer consists of two regions: an outer layer, rich in Cr and Ti (primarily $Cr_2O_3$ and TiO mixtures), and an inner layer, namely a dense $Al_2O_3$ layer with substrate protrusions, enhancing adhesion and preventing spallation (Table 4). $Al_2O_3$ is distributed in two modes: uniformly at the $Cr_2O_3$/substrate interface, improving layer compactness, and with root-like extensions into the substrate, acting as "pegs" to strengthen adhesion.

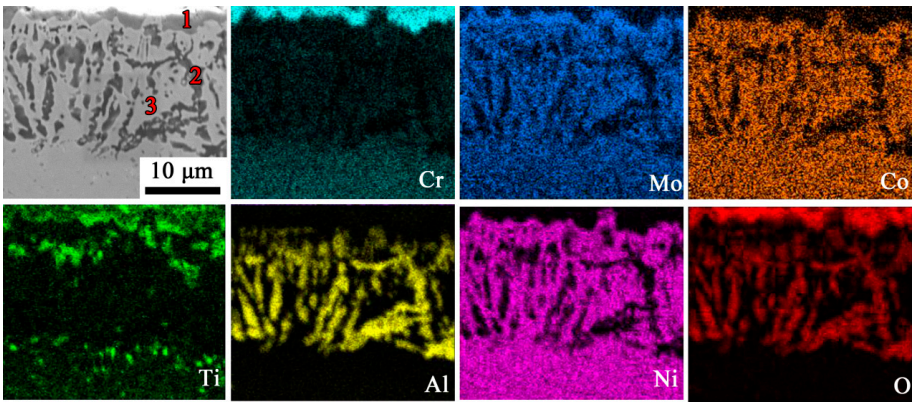


**Figure 12.** SEM images of a cross-section and EDS element mapping of the WGBR oxidized at 1000 °C for 1440 min. Point 1 consists of the outermost gray oxide layer, Point 2 exhibits a middle layer of dark gray dendritic oxide structures, and Point 3 corresponds to the light gray matrix phase.

**Table 4.** EDS analysis of the oxide scales in Figure 12 (at.%).

| Spots | Element (at.%) | | | | | | | | |
|---|---|---|---|---|---|---|---|---|---|
| | O | Al | Ti | Cr | Nb | Ni | Zr | Co | Mo |
| 1 | 54.44 | 0.93 | 5.70 | 33.06 | 12.22 | 2.02 | 1.31 | -- | -- |
| 2 | 59.91 | 21.55 | 11.43 | 3.64 | -- | 2.50 | 0.96 | -- | -- |
| 3 | -- | 5.91 | 3.27 | 11.36 | -- | 66.15 | -- | 9.74 | 3.56 |

Localized Nb enrichment in the oxide layer suggests $Nb_2O_5$ formation. Research [24] indicates that Nb oxidizes preferentially (oxygen potential: −146.2 kJ/mol, oxygen partial pressure: $8.1 \times 10^{-21}$ Pa) compared to Cr (−139.6 kJ/mol, $1 \times 10^{-19}$ Pa). Nb enhances $Cr_2O_3$ layer densification, reducing oxygen diffusion and vacancy defects. Mo shows no segregation, likely forming volatile $MoO_3$, while Co's low reactivity and slow diffusion

delay its oxidation. Studies [25] report Co only diffuses into oxide layers after prolonged exposure (e.g., 28 days at 850 °C in IN617 alloy).

To further validate the phase composition of oxides in the WGBR, FIB-TEM techniques were employed to analyze the cross-section of the oxide film. Figure 13 shows the FIB-SEM cross-section morphology of various oxide layers in the WGBR after oxidation for 1440 min at 1000 °C. The prepared sample was ion-thinned to below 100 nm and then analyzed using transmission electron microscopy. A detailed phase analysis of the oxide layer interface is illustrated in Figure 14 through TEM and high-resolution transmission electron microscopy (HRTEM) observations.

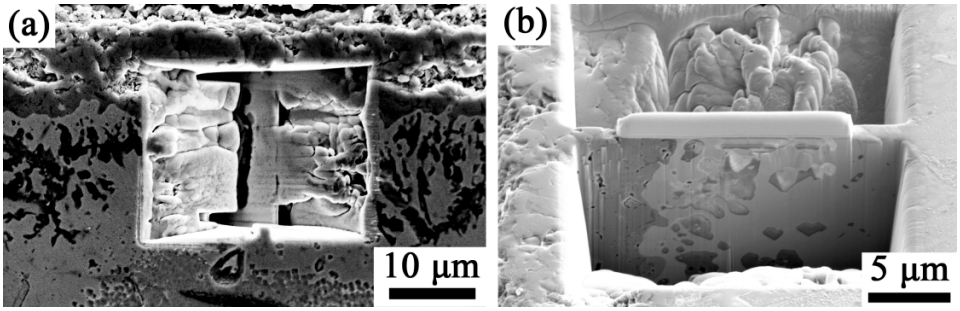


**Figure 13.** The FIB-SEM cross-section morphology (**a**) and high-magnification FIB-SEM micrograph (**b**) of various oxide layers in the WGBR after oxidation for 1440 min at 1000 °C.

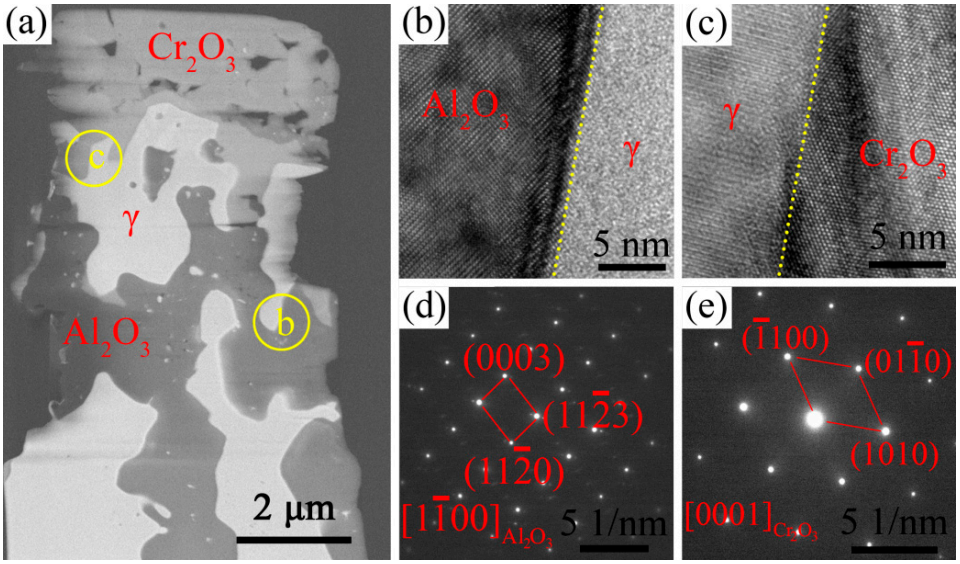


**Figure 14.** Images of a cross-section: (**a**) BF image near the interface of scale and substrate, (**d**) SAD patterns of $Al_2O_3$, (**e**) SAD patterns of $Cr_2O_3$, and (**b**,**c**) HRTEM image of the yellow circles in (**a**).

Figure 14a reveals distinct contrast differences between the inner and outer layers of the oxidation products in the WGBR. The TEM morphology from top to bottom in Figure 14a corresponds to the SEM morphology in Figure 10c. Indexing of transmission diffraction patterns from the outer and inner layers indicates that the dense outer layer primarily consists of $Cr_2O_3$ oxide, while the uniformly distributed inner layer is predominantly $Al_2O_3$ oxide. Further analysis of the interfacial relationships between these oxides and the substrate demonstrates no distinct orientation relationship between $Cr_2O_3$ and the substrate phase, nor between $Al_2O_3$ and the substrate phase.

## 4. Discussion

### *4.1. High-Temperature Oxidation Mechanism*

Based on the aforementioned results, the oxidation behaviors of the BM and WGBR at 1000 °C can be schematically summarized as shown in Figure 15. The oxidation processes of both the BM and WGBR comprise two stages: initial oxidation and steady-state oxidation.

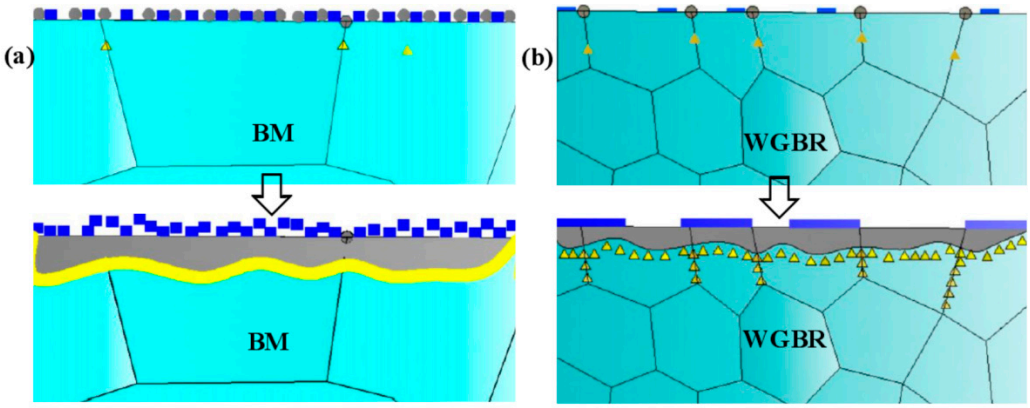


**Figure 15.** Schematic diagram showing the oxidation processes of the BM (**a**) and WGBR (**b**).

As illustrated in Figure 15a, during the initial stage, selective oxidation of Ni dominates in BM, accompanied by minor oxidation of Cr and Ti. The primary oxidation products at this stage are NiO, $Cr_2O_3$, and $TiO_2$. Upon entering the steady-state stage, the dense oxide layer formed by NiO and $Cr_2O_3$ isolates the substrate from direct oxygen contact, shifting the oxidation kinetics to ion diffusion control through the $Cr_2O_3$ layer. $Ni^{2+}$ and $Ti^{4+}$ ions diffuse outward, leading to the formation of NiO and $TiO_2$ on the $Cr_2O_3$ surface. Concurrently, NiO reacts with $Cr_2O_3$ to form $NiCr_2O_4$ spinel. Oxygen ions ($O^{2-}$) continue diffusing inward, combining with $Cr^{3+}$ to thicken the $Cr_2O_3$ layer and with $Al^{3+}$ to form coarsened $Al_2O_3$ particles. The embedding of initial oxide particles into the $Cr_2O_3$ layer enhances interfacial adhesion.

Figure 15b depicts the oxidation process of the WGBR. In the initial stage, oxygen directly oxidizes Ni, Cr, and Ti, forming discrete $Cr_2O_3$, NiO, and $TiO_2$ particles. During the steady-state stage, the process transitions to diffusion-controlled kinetics. $Ni^{2+}$, $Al^{3+}$, and $Ti^{4+}$ ions diffuse outward, generating a dense $Cr_2O_3$ layer and localized $Al_2O_3$ domains. Compared to BM, WGBR exhibits higher Cr oxidation propensity, favoring the formation of a continuous $Cr_2O_3$ layer that significantly improves oxidation resistance. In contrast, BM undergoes more extensive Ni oxidation, resulting in a thicker but less protective oxide layer.

The green phase represents nickel oxide (NiO), the gray phase indicates chromium oxide ($Cr_2O_3$), and the yellow phase corresponds to aluminum oxide ($Al_2O_3$).

With the continuous migration of oxygen from the surface to the substrate, oxide films of varying morphologies and thicknesses form in a specific sequence. During the initial oxidation stage, oxygen diffusion leads to the formation of a NiO oxide film with lower Gibbs free energy:

$$G_T^\theta\left(kJmol^{-1}\right) = -468.0892 + 0.1696T(K) \quad (3)$$

Subsequently, a $Cr_2O_3$ interlayer forms, whose Gibbs free energy is

$$\Delta G_T^\theta\left(kJmol^{-1}\right) = -752.4631 + 0.1684T(K) \quad (4)$$

Within the oxide film structure, the Gibbs free energy of the $TiO_2$ interlayer is expressed as

$$\Delta G_T^\theta\left(kJmol^{-1}\right) = -944.75 + 0.1854T(K) \quad (5)$$

Meanwhile, the Gibbs free energy of the $Al_2O_3$ interlayer is

$$\Delta G_T^{\theta}\left(\mathrm{kJmol^{-1}}\right) = -1127.3137 + 0.2193\mathrm{T(K)} \quad (6)$$

The high-temperature oxidation behavior of the WGBR reveals that its oxide layer consists of a protective $Cr_2O_3$ layer, a non-protective $TiO_2$ layer, and $NiCr_2O_4$. These findings align with XRD analysis results. Notably, $NiCr_2O_4$ is spontaneously generated through the following reaction between NiO and $Cr_2O_3$:

$$\mathrm{NiO{+}Cr_2O_{3(g)} = NiCr_2O_{4(s)},}\ \Delta G_T^{\theta}\left(\mathrm{kJmol^{-1}}\right) = -1378.26 + 0.3677\mathrm{T(K)} \quad (7)$$

The BM and WGBR exhibit significantly more intense oxidation behavior at 1100 °C compared to 900 °C and 1000 °C, indicating a transition in oxidation mechanisms within the 1000–1100 °C temperature range. Elevated temperatures naturally enhance the diffusion of chromium, titanium, and oxygen, leading to accelerated mass gain and oxidation rates. Crucially, non-protective $NiCr_2O_4$ forms after 1440 min of oxidation at 1100 °C. The formation of $NiCr_2O_4$ consumes the protective $Cr_2O_3$ layer, exacerbating oxidation progression and ultimately causing severe oxidative degradation. Thus, the emergence of $NiCr_2O_4$ is a critical factor influencing oxidation behavior at 1100 °C. Additionally, as highlighted by Kumar et al. [26], the outer $Cr_2O_3$ layer can be further oxidized into gaseous $CrO_3$ at elevated temperatures. Since $CrO_3$ is volatile and non-protective, this secondary oxidation of $Cr_2O_3$ represents another key contributor to the severe oxidation observed at 1100 °C.

### *4.2. Oxide Spallation Mechanism Analysis*

Figure 14 shows the surface morphology of the BM after oxidation at 1000 °C for 1440 min. As observed, the surface oxide layer (NiO) on the BM exhibits cracking and spallation following oxidation at 1000 °C for 1440 min. Based on the BM's microstructure, a schematic diagram of the growth, cracking, and spallation of the NiO oxide layer is proposed, as illustrated in Figure 16.

Thermodynamic calculations of the Gibbs free energy for oxide formation by the BM's constituent elements reveal that NiO has the lowest free energy, explaining its preferential formation on the BM surface (Figure 16a). As temperature increases, oxide growth occurs through interconnected networks, forming a thin and uniform oxide layer (Figure 16b), accompanied by internal stress development. Stress relief via oxide debonding at the oxide/substrate interface primarily occurs at defect sites (e.g., Kirkendall voids) (Figure 16c). While this expansion process does not accelerate oxidation rates, prolonged exposure to elevated temperatures or extended durations leads to gradual nodular growth of the oxide scale. Notably, such expansion partially relaxes compressive stresses, resulting in localized bulging. When the oxide scale becomes excessively thick, preventing the relief of compressive stresses through deformation or wrinkling, cracks initiate at defect sites (Figure 16d). These cracks propagate under accumulating stress, eventually causing severe spallation. Post-spallation, deformed oxide scales remain with clearly visible scale/alloy interfaces. An analysis indicates that weak bonding strength at the scale/alloy interface is the primary cause of cracking and spallation. To address this, improving interfacial adhesion strength is crucial for enhancing the oxidation resistance of BM alloys [27].

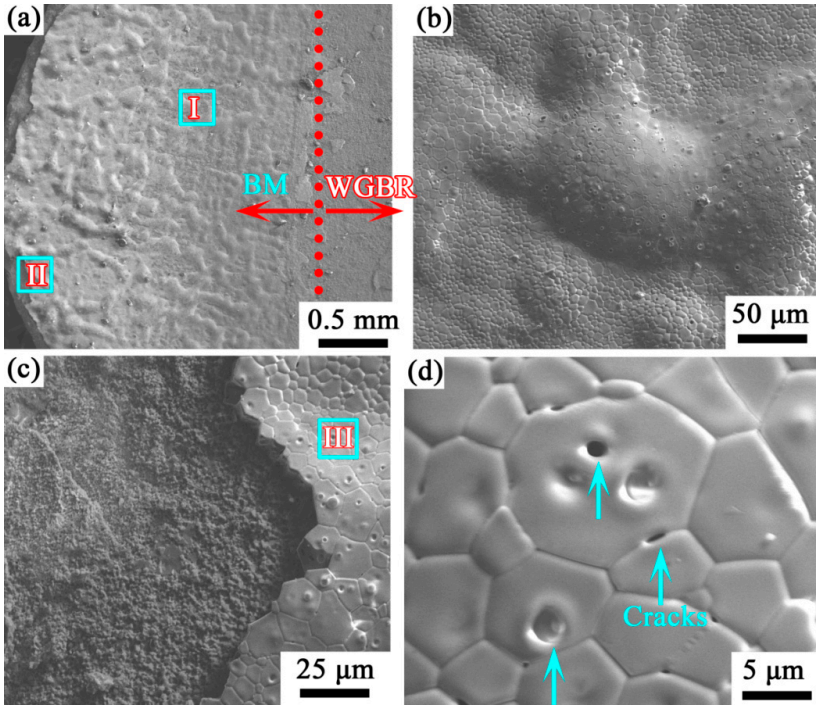


**Figure 16.** (**a**) SEM images of the oxide scales of the joint after oxidation for 1440 min at 1000 °C, (**b**) magnification of I in (**a**), (**c**) magnification of II in (**a**), (**d**) magnification of III in (**c**).

Spallation during oxidation is primarily driven by two factors: thermal stress, generated during heating and cooling cycles, arising from the mismatch in coefficients of thermal expansion (CTEs) between the oxide scale and the substrate, and growth stress, caused by the volumetric difference between the formed oxide and the consumed metal. Thermal cycling also introduces cracks in the oxide layer, further enhancing oxygen supply to the substrate. The spallation behavior depends on the grain size of the base material undergoing oxidation. Due to CTE mismatch, the surface NiO layer tends to fracture into powdery structures under stress, while the intermediate $Cr_2O_3$ layer retains a dense, protective morphology.

Figure 17 shows the surface morphology of the WGBR after oxidation at 800 °C for 1440 min. During initial oxidation, $Cr_2O_3$ oxides preferentially precipitate at grain boundaries due to their high density in the WGBR. As temperature and oxidation time increase, $Cr_2O_3$ rapidly covers the alloy surface, forming a dense protective layer. This grain boundary oxidation behavior aligns with observations in nickel-based superalloys, where grain boundaries act as fast diffusion pathways in gaseous environments, making intergranular oxide layers prevalent. $Cr_2O_3$ growth initiates along grain boundaries, consistent with findings in this study.

Figure 18 illustrates the grain boundary oxidation mechanism in the WGBR. Initially, oxides grow along grain boundaries intersecting the surface. Although thermodynamic calculations predict NiO as the most stable phase (lowest Gibbs free energy), kinetic factors dominate: grain boundaries, as high-energy regions, provide preferential diffusion pathways for Cr, enabling rapid $Cr_2O_3$ formation [28]. High growth stresses near grain boundaries arise from two effects: thicker oxide layers along boundaries in fine-grained materials, amplifying the volumetric mismatch between oxides and the consumed metal, and physical barriers formed between oxides growing along boundaries and intragranular regions [29,30]. These combined factors promote the rapid formation of a dense $Cr_2O_3$ oxide film on the alloy surface, significantly enhancing oxidation resistance

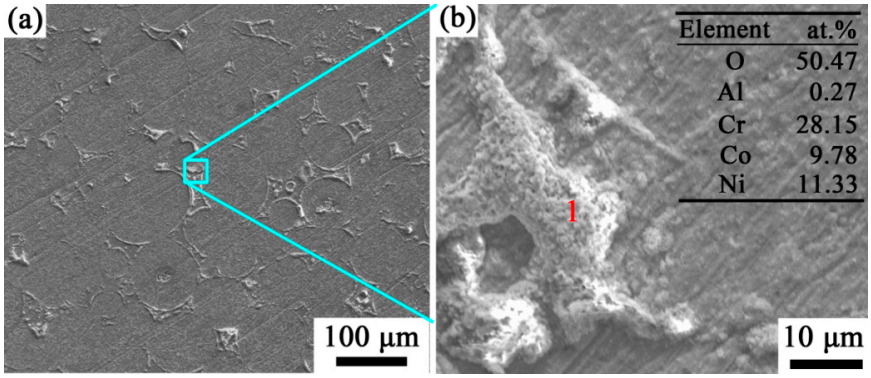


**Figure 17.** (**a**) SEM images of the oxide scales of the WGBR after oxidation for 1440 min at 800 °C, (**b**) high-magnification SEM micrograph of the blue-framed region in Figure 17 (**a**). The EDS spectrum of the light gray region (Point 1) is presented in the upper-right corner of Figure 17 (**b**).

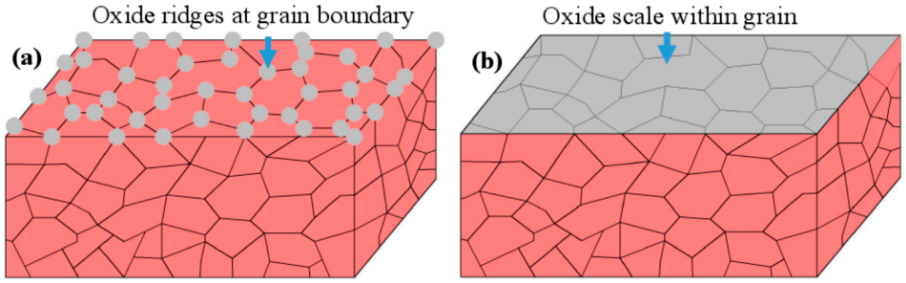


**Figure 18.** Schematic showing (**a**) oxide ridge formation occurring initially along the grain boundary and (**b**) the growth of oxide within the grain and lateral growth of the oxide ridge.

## 5. Conclusions

This oxidation kinetics study revealed that the large-gap powder metallurgy joint zone exhibits superior oxidation resistance compared to the base material at 1000 °C and above, with their oxidation weight gain versus time curves both following parabolic laws. This phenomenon can be attributed to the fact that the preferentially formed NiO on the base material surface lacks stable oxidation resistance and tends to spall off, accompanied by partial oxidation of Cr and Ti elements, where the primary oxidation products are NiO and $TiO_2$. In contrast, the large-gap powder metallurgy joint zone, characterized by abundant grain boundaries, forms dense $Cr_2O_3$ during the initial oxidation stage, thereby significantly enhancing its oxidation resistance at 1000 °C.

**Author Contributions:** Z.C.: Writing—Original Draft, Software, Methodology, Investigation, Formal Analysis, Data Curation, Conceptualization. X.L. (Xin Lai): Writing—Review and Editing, Writing—Original Draft, Methodology. J.F.: Resources, Investigation, Formal Analysis. Zhengyi Jin: Visualization, Validation, Methodology. J.H.: Writing—Review and Editing, Visualization, Supervision, Resources. X.L. (Xiaoqiang Li): Writing—Review and Editing, Visualization, Validation, Supervision, Resources, Funding Acquisition. F.L.: Writing—Review and Editing, Writing—Original Draft, Supervision, Resources, Methodology. All authors have read and agreed to the published version of the manuscript.

**Funding:** South China University of Technology Fundamental Research Funds for the Central Universities (No. 2023ZYGXZR005), Key Areas Research Program for Higher Education Institutions of Guangdong Provincial Department of Education (No. 2023ZDZX3058), The 17th "Challenge Cup" Guangdong University Students' Extracurricular Academic Science and Technology Works Competition & 2023 Guangdong Provincial Science and Technology Innovation Strategy Special Funds ("Climbing Program") University-level Cultivation Project (No. 2023SCPY032), 2023 Guangdong Provincial Science and Technology Innovation Strategy Special Funds (University Students' Science

and Technology Innovation Cultivation) (No. pdjh2023b0823), Guangdong Basic and Applied Basic Research Foundation Project (No. 2023A1515010384), School-Level Research Project of Guangdong Polytechnic of Industry and Commerce (No. 2024-ZKT-05), Guangzhou Science and Technology Bureau Projects (No. SL2022A04J00030).

**Data Availability Statement:** The original contributions presented in the study are included in the article; further inquiries can be directed to the corresponding authors.

**Acknowledgments:** This research was funded by South China University of Technology Fundamental Research Funds for the Central Universities (No. 2023ZYGXZR005), Guangdong Basic and Applied Basic Research Foundation Project (No. 2023A1515010384) and School-Level Research Project of Guangdong Polytechnic of Industry and Commerce (No. 2024-ZKT-05). Zhun Cheng acknowledges funding from the Key Areas Research Program for Higher Education Institutions of Guangdong Provincial Department of Education (No. 2023ZDZX3058), The 17th "Challenge Cup" Guangdong University Students' Extracurricular Academic Science and Technology Works Competition & 2023 Guangdong Provincial Science and Technology Innovation Strategy Special Funds ("Climbing Program") University-level Cultivation Project (No. 2023SCPY032), and 2023 Guangdong Provincial Science and Technology Innovation Strategy Special Funds (University Students' Science and Technology Innovation Cultivation) (No. pdjh2023b0823). Hansheng Yan and Bo Wei contributed to the analyses and discussion of results and reviewed the entire manuscript.

**Conflicts of Interest:** No conflicts of interest exist in the submission of this manuscript, and the manuscript is approved by all authors for publication.

## References

1. Cheng, Z.; Li, X.Q.; Wang, B.; Qu, S.G.; Li, H.Y. $M_3B_2$-type borides effect on the wide gap brazing of K417G alloy with mixed powder. *J. Alloys Compd.* **2020**, *821*, 153431. [CrossRef]
2. Yu, X.F.; Wang, S.J.; Zheng, D.Y.; Shen, X.; Li, Y.; Liu, W.; Su, Y.; Liu, F. Effect of heat treatment on rotating bending fatigue properties of K417G nickel-base superalloy. *J. Alloys Compd.* **2022**, *905*, 164209. [CrossRef]
3. Zhang, G.T.; Liu, W.J.; Bian, H.Y.; Wang, C.; Li, Q.; Wang, H. Evolutionary mechanism analysis of Laves phase precipitation behavior and wear resistance of laser-directed energy deposited T-800 alloy coatings on K417G alloy at various aging temperatures. *Mater. Lett.* **2025**, *382*, 137938. [CrossRef]
4. Liu, S.; Liu, C.S.; Gao, X.Y.; Wen, X.; Qiao, S.; Yuan, C. Insights into process optimization and induction preheating for crack-free laser metal deposition of nickel-based superalloy K417G. *J. Mater. Res. Technol.* **2024**, *29*, 2035–2050. [CrossRef]
5. Zhang, L.H.; Liu, Y.H.; Guo, H.M.; Xing, W. Effects of pouring temperature on microstructure and properties of K417G superalloy in thermally-controlled solidification process. *Rare Met. Mater. Eng.* **2024**, *53*, 2546–2554.
6. Kalfhaus, T.; Schneider, M.; Ruttert, B.; Sebold, D.; Hammerschmidt, T.; Frenzel, J.; Drautz, R.; Theisen, W.; Eggeler, G.; Guillon, O.; et al. Repair of Ni-based single-crystal superalloys using vacuum plasma spray. *Mater. Des.* **2019**, *168*, 107656. [CrossRef]
7. Way, M.; Willingham, J.; Goodall, R. Brazing filler metals. *Int. Mater. Rev.* **2019**, *65*, 1–29. [CrossRef]
8. Cheng, Z.; Li, X.Q.; Qu, S.G.; Zhu, D.; Li, H. Microstructural evolution and mechanical properties of wide gap brazing of K417G superalloy. *Rare Met. Mater. Eng.* **2021**, *50*, 3262–3269.
9. Ren, X.Y.; Wang, H.; Li, W.W.; Dong, Q.; Chen, B.; Mao, W. Efect of holding time on interfacial evolution and mechanical strength of wide-gap brazed K417G superalloy joints. *Weld. World* **2024**, *68*, 3079–3084. [CrossRef]
10. Li, Y.; Tan, Y.; You, X.Q.; Wang, D.; Hu, Y.; Song, S.; Qiang, J. Effect of trace impurity elements on the high-temperature oxidation resistance of a high-purity nickel-based superalloy. *Corros. Sci.* **2023**, *211*, 110904. [CrossRef]
11. Miller, C.F.; Simmons, G.W.; Wei, R.P. High temperature oxidation of Nb, NbC and $Ni_3Nb$ and oxygen enhanced crack growth. *Scr. Mater.* **2000**, *42*, 227–232. [CrossRef]
12. Zhao, D.; Xuan, W.D.; Shao, G.L.; Che, X.; Wang, S.; Qi, J.; Ren, Z. Unveiling the short-term oxidation behavior of nickel-base superalloy CMSX-4 in high-temperature air. *Corros. Sci.* **2025**, *251*, 112915. [CrossRef]
13. Khedr, M.; Li, W.; Min, N. Strengthening contributions of mechanical twinning and dislocations to the flow stress of hadfield high-manganese steel: Quantitative analysis. *J. Mater. Eng. Perform.* **2022**, *32*, 501–511. [CrossRef]
14. Cheng, Z.; Li, X.Q.; Zhang, M.A.; Qu, S.; Li, H. Wide-gap brazing of K417G alloy assisted by in situ precipitation of M3B2 boride particle. *Materials* **2020**, *13*, 3140. [CrossRef]
15. He, W.B.; Xue, Z.L.; Guo, R.; Chen, N. On machining K417 superalloy with sliding self-propelled rotary tools: Simulation and experimental investigation. *Int. J. Adv. Manuf. Technol.* **2023**, *126*, 1669–1680. [CrossRef]

16. Li, X.Q.; Cheng, Z.; Qu, S.G.; Zhu, D.; Li, H. Effect of filler metal on the microstructural evolution and mechanical properties of wide gap brazed K417G superalloy joints. *Vacuum* **2021**, *184*, 109967. [CrossRef]
17. Jang, C.; Kim, D.; Kim, D.; Sah, I.; Ryu, W.S.; Yoo, Y.S. Oxidation behaviors of wrought nickel-based superalloys in various high temperature environments. *Trans. Nonferr. Met. Soc. China* **2011**, *21*, 1524–1531. [CrossRef]
18. Liu, B.C.; Li, H.; Lou, L.H. Isothermal Oxidation Behavior of Single-Crystal Nickel-Base Superalloy DD10. *Rare Met. Mater. Eng.* **2010**, *39*, 1407–1410.
19. Xu, C.; Nai, Q.L.; Yao, Z.H.; Dong, J. Grain Boundary Oxidation Effect of GH4738 Superalloy on Fatigue Crack Growth. *Acta Metall. Sin.* **2017**, *53*, 44–51.
20. Wang, Y.L.; Tan, Y.; Liu, L.B.; Li, P.; Li, X. Oxidation behavior and mechanism of GH4975 superalloy prepared electron beam smelting between 900 °C and 1100 °C in air. *Vacuum* **2024**, *219*, 112752. [CrossRef]
21. Wang, Q.; Shuai, S.X.; Lu, G.X.; Attard, B.; Ma, R.; Gao, S.; Rochman, A.; Cassar, G. Residual stress release and corresponding microstructural changes in high-energy impact-modified GH4169 after aging at 425 °C and 650 °C. *J. Mater. Res. Technol.* **2024**, *33*, 6461–6466. [CrossRef]
22. Shi, Z.X.; Yan, X.F.; Duan, C.H. Isothermal oxidation behavior of newly developed superalloy GH4282. *Trans. Nonferr. Met. Soc. China.* **2019**, *44*, 45–53.
23. Gao, S.; Hou, J.S.; Yang, F.; Wang, C.S.; Zhou, L.Z. High Temperature Oxidation Behaviors of Two Cast Ni-based Superalloys. *Rare Met. Mater. Eng.* **2019**, *48*, 960–966.
24. Li, Y.; Liu, X.G.; Guo, J.T.; Yuan, C.; Yang, H.C. Isothermal oxidation behavior of cast Ni-base superalloy K44. *Trans. Nonferr. Met. Soc. China.* **2006**, *16*, 1967–1972.
25. Zheng, L.; Zhang, M.C.; Dong, J. Oxidation behavior and mechanism of powder metallurgy Rene95 nickel based superalloy between 800 and 1000 C. *Appl. Surf. Sci.* **2010**, *256*, 7510–7515. [CrossRef]
26. Kumar, D.; Adharapurapu, R.R.; Pollock, T.M.; Was, G.S. High-Temperature Oxidation of Alloy 617 in Helium Containing Part-Per-Million Levels of CO and $CO_2$ as Impurities. *Met. Mater. Trans. A* **2011**, *42*, 1245–1265. [CrossRef]
27. Zheng, L.; Zhang, M.; Chellali, R.; Dong, J. Investigations on the growing, cracking and spalling of oxides scales of powder metallurgy Rene95 nickel-based superalloy. *Appl. Surf. Sci.* **2011**, *257*, 9762–9767. [CrossRef]
28. Athreya, C.N.; Deepak, K.; Kim, D.I.; de Boer, B.; Mandal, S.; Sarma, V.S. Role of grain boundary engineered microstructure on high temperature steam oxidation behaviour of Ni based superalloy alloy 617. *J. Alloys Compd.* **2019**, *778*, 224–233. [CrossRef]
29. Ma, J.Y.; Jiang, W.X.; Wang, J. Initial oxidation behavior of a single crystal superalloy during stress at 1150 °C. *Sci. Rep.* **2020**, *10*, 3089. [CrossRef]
30. Bitara, T.E.; Meligya, M.E.; Khedrb, M. Investigation of exhaust valve failure in a marine diesel engine. *Eng. Fail. Anal.* **2020**, *114*, 104574. [CrossRef]

**Disclaimer/Publisher's Note:** The statements, opinions and data contained in all publications are solely those of the individual author(s) and contributor(s) and not of MDPI and/or the editor(s). MDPI and/or the editor(s) disclaim responsibility for any injury to people or property resulting from any ideas, methods, instructions or products referred to in the content.